



Irwin, P. G. J., Toledo, D., Garland, R., Teanby, N. A., Fletcher, L. N., Orton, G. A., & Bézard, B. (2018). Detection of hydrogen sulfide above the clouds in Uranus's atmosphere. *Nature Astronomy*, 2(5), 420-427. <https://doi.org/10.1038/s41550-018-0432-1>

Peer reviewed version

Link to published version (if available):  
[10.1038/s41550-018-0432-1](https://doi.org/10.1038/s41550-018-0432-1)

[Link to publication record in Explore Bristol Research](#)  
PDF-document

This is the author accepted manuscript (AAM). The final published version (version of record) is available online via Nature at <https://www.nature.com/articles/s41550-018-0432-1> . Please refer to any applicable terms of use of the publisher.

## University of Bristol - Explore Bristol Research

### General rights

This document is made available in accordance with publisher policies. Please cite only the published version using the reference above. Full terms of use are available:  
<http://www.bristol.ac.uk/red/research-policy/pure/user-guides/ebr-terms/>

# Detection of hydrogen sulphide (H<sub>2</sub>S) above the clouds in Uranus' atmosphere

Patrick G. J. Irwin<sup>1</sup>, Daniel Toledo<sup>1</sup>, Ryan Garland<sup>1</sup>, Nicholas A. Teanby<sup>2</sup>, Leigh N. Fletcher<sup>3</sup>, Glenn A. Orton<sup>4</sup>, & Bruno Bézard<sup>5</sup>

<sup>1</sup>*Department of Physics (Atmospheric, Oceanic and Planetary Physics), University of Oxford, Parks Rd, Oxford, OX1 3PU, UK.*

<sup>2</sup>*School of Earth Sciences, University of Bristol, Wills Memorial Building, Queens Road, Bristol, BS8 1RJ, UK.*

<sup>3</sup>*Department of Physics & Astronomy, University of Leicester, University Road, Leicester, LE1 7RH, UK.*

<sup>4</sup>*Jet Propulsion Laboratory, California Institute of Technology, 4800 Oak Grove Drive, Pasadena, CA 91109, USA*

<sup>5</sup>*LESIA, Observatoire de Paris, PSL Research University, CNRS, Sorbonne Universités, UPMC Univ. Paris 6, Université Paris-Diderot, Sorbonne Paris Cité, 5 place Jules Janssen, 92195 Meudon, France.*

**The main cloud deck on Uranus is observed from visible to near-infrared observations to have a cloud-top pressure of somewhere between 1.2 and 3 bar. However, its composition has never been unambiguously identified, although it is widely assumed to be composed primarily of either ammonia (NH<sub>3</sub>) or hydrogen sulphide (H<sub>2</sub>S) ice. Here we present evidence of a clear detection of gaseous H<sub>2</sub>S above this cloud deck in the wavelength region 1.57 – 1.59 μm**

with a mole fraction of 0.4 – 0.8 ppm at the cloud tops. Its detection constrains the deep bulk sulphur/nitrogen abundance to exceed 4.4 – 5.0 times the solar value in Uranus’ bulk atmosphere, and places a lower limit on the mole fraction of H<sub>2</sub>S below the observed cloud of  $(1.0 - 2.5) \times 10^{-5}$ . The detection of gaseous H<sub>2</sub>S at these pressure levels adds to the weight of evidence that the principal constituent of 1.2 – 3-bar cloud is likely to be H<sub>2</sub>S ice.

In the absence of any spectrally identifiable ice absorption features, the identity of the main component of the cloud in Uranus’ atmosphere with cloud top pressure 1.2 – 3 bar<sup>1-3</sup> has long been a source of debate, although authors have most commonly ascribed it to be composed of either ammonia (NH<sub>3</sub>) or hydrogen sulphide (H<sub>2</sub>S) ice<sup>3</sup>. This is based on the assumed presence at deeper pressures ( $\sim 40$  bar) of an ammonium hydrosulphide (NH<sub>4</sub>SH) cloud, which combines together in equal parts any available H<sub>2</sub>S and NH<sub>3</sub>, leaving the remaining more abundant molecule to condense alone at lower pressures<sup>4</sup>. Deeper in the atmosphere (20 – 40 bar), observations of Uranus and Neptune at microwave wavelengths (1 – 20 cm) with the Very Large Array (VLA)<sup>5</sup> found that there was a missing component of continuum absorption, which was concluded to be likely due to the pressure-broadened wings of H<sub>2</sub>S lines with wavelengths of less than a few mm. The deep abundance of H<sub>2</sub>S was estimated to be 10 – 30 $\times$  solar and this analysis further concluded, building upon previous studies<sup>6,7</sup>, that the bulk S/N ratio must exceed  $\sim 5\times$  the assumed solar ratio<sup>8</sup> in order that the bulk abundance of H<sub>2</sub>S exceeds that of NH<sub>3</sub>, leaving residual H<sub>2</sub>S above the deeper NH<sub>4</sub>SH cloud. Hydrogen sulphide is believed to be a significant component of all the giant planet atmospheres and has been detected *in situ* in Jupiter’s deep atmosphere by the Galileo probe mass spectrometer<sup>9</sup> (and also in comets, both *in situ* and remotely<sup>10,11</sup>). However,

it has never been unambiguously remotely detected in the atmospheres of any of the giant planets, aside from a possible debated detection in Jupiter’s atmosphere following the impact of Comet Shoemaker-Levy 9 in 1994<sup>12,13</sup>. Hence, while H<sub>2</sub>S is probably the source of the missing continuum absorption at microwave wavelengths in Uranus and Neptune’s atmospheres, and is also probably the main component of the 1.2 – 3-bar cloud, it has never been unequivocally detected in Uranus’ atmosphere to confirm this.

Detection of H<sub>2</sub>S and NH<sub>3</sub> absorption features at thermal-IR wavelengths is very challenging due to the extremely cold atmospheric temperatures in Uranus’ atmosphere, but at visible/near-infrared wavelengths, there are weak absorption bands that could potentially be detected in sunlight reflected from the cloud tops at wavelengths where the absorption of other gases is weak. The available line data for the key condensable volatiles in Uranus’ atmosphere (i.e. CH<sub>4</sub>, NH<sub>3</sub>, H<sub>2</sub>S) have recently been greatly improved and, although these absorptions are weak, we looked to see whether we could detect these features in near-IR ground-based high resolution spectroscopic measurements.

Observations of Uranus (with adaptive optics) were made with Gemini-North’s Near-infrared Integral Field Spectrometer (NIFS) instrument in 2009/2010<sup>14,15</sup>. NIFS records 3'' × 3'' image ‘cubes’ with a pixel size of 0.103 × 0.043'', where each pixel is a spectrum covering, in the H-band, the wavelength range 1.476 – 1.803 μm with a spectral resolution of R = 5290. For this study we used observations recorded on 2nd November 2010 at approximately 06:00UT<sup>15</sup>. To minimise random noise we averaged the observations over seven 5 × 5 pixel boxes, indicated in Fig. 1 and

listed in Table 1. We selected the wavelength region  $1.49 - 1.64 \mu\text{m}$  for our analysis, comprising  
 $n_y = 937$  spectral points. We initially set the noise at each wavelength to be the variance of data  
 in these  $5 \times 5$  pixel boxes. However, we found that we were not quite able to fit these spectra to  
 a precision of  $\chi^2/n_y \sim 1$  and attributed this to unknown deficiencies in our spectral modelling.  
 We thus multiplied these errors by a single factor of 1.6 at all wavelengths (except for area ‘6’, for  
 which the variance was already sufficiently large) to account for these ‘forward-modelling’ errors.  
 For our reference spectrum we chose the region close to the disc centre, centred at  $15.3^\circ\text{N}$  (Area  
 ‘1’), but performed the same analysis for all other selected regions, reported in the supplementary  
 material.

To model the observed spectra we used the NEMESIS<sup>16</sup> retrieval model, using the correlated-  
 k approximation with ‘k’-tables generated from the recently published WKLMC@80K+<sup>17</sup> line  
 data for  $\text{CH}_4$  and updated line data for  $\text{H}_2\text{S}$  and  $\text{NH}_3$  from HITRAN2012<sup>18</sup>. The mean absorption  
 strengths of  $\text{CH}_4$ ,  $\text{NH}_3$  and  $\text{H}_2\text{S}$  across the H-band wavelength range contained in these data (cal-  
 culated at 100 K and 1 atm) are shown in Fig. 1. Our *a priori* vertical atmospheric profile was  
 based on the ‘F1’ temperature profile, determined from HST/STIS and Voyager 2 observations<sup>3</sup>.  
 This profile has a deep methane mole fraction of 4%<sup>19</sup>, and has a varying relative humidity with  
 height above the condensation level. The  $\text{He}:\text{H}_2$  ratio was set to 0.131 and the profile includes  
 0.04% mole fraction of  $\text{Ne}^3$ . To this profile we added  $\text{NH}_3$  and  $\text{H}_2\text{S}$ , assuming arbitrary ‘deep’  
 mole fractions (i.e. above the putative  $\text{NH}_4\text{SH}$  cloud) of 0.1% for both, and limited their abun-  
 dance to not exceed the saturated vapour pressure<sup>20</sup> in the troposphere as the temperature falls with  
 height, adjusting the abundance of hydrogen and helium (keeping  $\text{He}:\text{H}_2 = 0.131$ ) to ensure the

83 mole fractions summed to unity at each pressure level. Figure 2 shows the modelled abundance  
 84 profiles of the three condensible species falling with height. We can see that the saturated vapour  
 85 pressure of  $\text{H}_2\text{S}$  at the pressure of the main clouds of Uranus (1.2 – 3 bar) is approximately 2000  
 86 times higher than that of  $\text{NH}_3$ . Hence, even though the peak  $\text{NH}_3$  absorption strength in this spec-  
 87 tral region is, from Fig. 1,  $\sim 100$  times stronger than that of  $\text{H}_2\text{S}$ , we expect the absorption lines  
 88 of  $\text{H}_2\text{S}$  to be far more visible due to the higher likely abundance of  $\text{H}_2\text{S}$  and also the lines of  $\text{H}_2\text{S}$   
 89 having maximum strength at wavelengths of minimum methane opacity (Fig. 1). The very low  
 90 saturated vapour pressure of  $\text{NH}_3$  at the 1.2–3 bar level in Uranus’ atmosphere makes it likely that  
 91  $\text{NH}_3$  would not have enough abundance to condense into a cloud with sufficient opacity at this  
 92 level as has previously been noted<sup>3</sup>.

93 We fitted the spectrum using a multiple-scattering model and modelled cloud opacity with  
 94 a vertically continuous profile of particles (at 39 levels) with a Gamma size distribution of mean  
 95 radius  $1.0 \mu\text{m}$  and variance 0.05. This size distribution is typical of that assumed in previous  
 96 analyses<sup>2,21</sup>, but is an assumption and is not constrained by, for example, a microphysical model.  
 97 In addition, the assumption that the particles have the same size distribution at all altitudes is  
 98 an oversimplification since we would expect that in real clouds the particles would be smaller at  
 99 higher altitudes. However, the primary objective of this study was to search for the spectral sig-  
 100 nature of  $\text{H}_2\text{S}$  gas, rather than to fit a sophisticated cloud model and we thus chose a model that  
 101 would be simple and easy to fit. It should be noted that our simple cloud model is used to model  
 102 not only the effects of the main 1.2 – 3 bar cloud, but also any  $\text{CH}_4$  cloud opacity and any tropo-  
 103 spheric/stratospheric haze opacity that may be present. In addition to fitting the cloud opacity at

104 each level in the atmosphere, we also fitted the imaginary refractive index spectrum of the parti-  
 105 cles (assumed to be the same at all vertical levels) at nine wavelengths between 1.4 and 1.8  $\mu\text{m}$ ,  
 106 reconstructing the real part of the refractive index spectrum using the Kramers-Kronig relation<sup>21</sup>,  
 107 assuming  $n_{\text{real}} = 1.4$  at 1.6  $\mu\text{m}$ . We constrained the imaginary refractive index spectrum to vary  
 108 reasonably slowly with wavelength, to avoid degeneracy with the  $\text{H}_2\text{S}$  signal we were trying to de-  
 109 tect (see Methods). Self-consistent extinction cross-sections, single-scattering albedos and phase  
 110 functions were then computed at all wavelengths using Mie theory, with the phase functions ap-  
 111 proximated with Henyey-Greenstein functions (see Methods section). The total number of variable  
 112 parameters in our retrieval was thus  $n_x = 39 + 9 = 48$ , and thus the total number of degrees of  
 113 freedom,  $n = n_y - n_x$  was 889.

114 Figure 3 shows our fit to the reference Uranus spectrum (Area ‘1’ of Fig. 1 and Table 1)  
 115 when  $\text{H}_2\text{S}$  and  $\text{NH}_3$  absorption is neglected, using three different *a priori* values of the imaginary  
 116 refractive index of 0.001, 0.01 and 0.1, respectively, at all wavelengths with an *a priori* error  
 117 of  $\pm 50\%$ . We can see that reasonably good fits are achieved for all three cases, but that better  
 118 fits are achieved with higher *a priori* values, with similar results for  $n_i = 0.01$  and  $n_i = 0.1$   
 119 ( $\chi^2/n \sim 1.7$ ). For the  $n_i = 0.001$  case, a poorer fit is achieved ( $\chi^2/n \sim 1.9$ ) as the solution cannot  
 120 move far enough away from the *a priori* to properly fit the spectrum. As a result the retrieved  
 121 particles have low imaginary refractive index and so are more scattering, necessitating the cloud  
 122 profile opacity to reduce quickly at pressures greater than 2–3 bar to prevent significant reflection  
 123 from these levels. This is in stark contrast to the other two solutions, where  $n_i$  is much higher  
 124 ( $n_i \sim 0.06$ ), and where we find that the single-scattering albedo of the particles is  $\varpi = 0.7\text{--}0.8$  and

phase function asymmetry is  $g \sim 0.7$  across the observed spectral range (Supplementary Fig.1).  
 These retrieved single-scattering albedo and phase-function asymmetry values agree very well  
 with a limb-darkening analysis<sup>14</sup>, which used these same Gemini/NIFS data smoothed to a lower  
 resolution of FWHM = 0.004  $\mu\text{m}$  and older, lower-resolution methane absorption k-distribution  
 data<sup>22</sup>, and also with an analysis of Keck and HST images<sup>23</sup>, which recommended  $\varpi = 0.75$  and  
 $g = 0.7$ . An important consequence of the low single-scattering albedo of the retrieved particles is  
 that solar photons are quickly absorbed as they reach the cloud tops and so we do not see significant  
 reflection from particles residing at pressures greater than 2–3 bar. This can be seen in the retrieved  
 error bars for the cloud opacity profiles in Fig. 3 quickly relaxing back to their *a priori* value as  
 the pressure increases and the profiles for the higher  $n_i$  values tending smoothly back to their *a*  
*priori* opacity/bar values. As a result, although we can clearly detect the cloud-top pressure at these  
 wavelengths, we cannot tell where the base is and thus cannot differentiate between a vertically  
 thin cloud based at 2–3 bar, or a cloud that extends vertically down to several bars with the same  
 cloud-top pressure. We also note here that when the particles are constrained to be more scattering,  
 the peak of cloud opacity is at a lower pressure than for the case with more absorbing particles.  
 This phenomenon may help to explain why HST/STIS<sup>3</sup> retrievals, which assume the particles to  
 be more scattering, find the cloud tops to be at lower pressures (1.2 bar) than retrievals near 1.5  
 $\mu\text{m}$ <sup>1,2</sup>, which assume more absorbing particles and find cloud tops at 2–3-bar.

Figure 4 compares our best fits to the observed reference spectrum (Area ‘1’ at 15.3°N) in  
 the 1.56 – 1.60  $\mu\text{m}$  region, including or excluding H<sub>2</sub>S absorption. When H<sub>2</sub>S absorption is not in-  
 cluded, we find that there is a significant discrepancy between the measured and modelled spectra,



giving  $\chi^2/n = 1.71$ . This discrepancy is significantly reduced when H<sub>2</sub>S absorption is included and NEMESIS allowed to scale the abundance of H<sub>2</sub>S, achieving a much closer fit with  $\chi^2/n = 1.30$ . When H<sub>2</sub>S absorption is not included, there are several peaks in the difference spectrum (Fig. 4) that match perfectly the effect of including or excluding this gas in the spectral calculation. We examined the correlation between the expected H<sub>2</sub>S signal and this difference spectrum between 1.57 and 1.60  $\mu\text{m}$ , and found a Pearson correlation coefficient of 0.718 (indicating a strong correlation) and a Spearman rank correlation coefficient of 0.602, with a two-sided significance value of  $D = 6.88 \times 10^{-20}$ , which equates to a 9- $\sigma$ -level detection. We also tested the effect on the calculated spectrum of including or excluding 100% relative humidity of ammonia (NH<sub>3</sub>), but found that this was completely undetectable due to ammonia's extremely low abundances at these temperatures. In case the ammonia abundance in Uranus' atmosphere is in reality highly supersaturated, we also tested the effect on the calculated spectrum of supersaturating NH<sub>3</sub> by factor of 1000, also shown in Fig. 4. However, we found that the absorption features of NH<sub>3</sub> do not coincide at all well with the difference spectrum, with correlation coefficients of only 0.271 (Pearson) and 0.256 (Spearman), respectively. We thus conclude that NH<sub>3</sub> is not the source of the missing absorption. The correlation between the spectral discrepancy of the fit, when H<sub>2</sub>S is neglected, and the differences between the modelled spectra when H<sub>2</sub>S or NH<sub>3</sub> absorption is added are shown in Supplemental Fig. 2.

The retrieved relative humidity of the H<sub>2</sub>S profile needed to match the observed absorption features was  $113 \pm 12\%$ . Since the mole fraction of H<sub>2</sub>S decreases rapidly with height, this scaling factor is strongly weighted by the abundance of H<sub>2</sub>S just above the cloud tops, i.e. at 2–3 bar and

found to be 0.47 ppm, but is consistent with the H<sub>2</sub>S profile having 100% relative humidity in this  
 region. However, this conclusion depends upon both the assumed temperature profile, which sets  
 the saturated vapour pressure, and also the assumed methane profile, which affects the retrieved  
 cloud-top pressure and thus the peak pressure level (and thus local temperature) of sensitivity  
 to H<sub>2</sub>S. To test these effects we repeated our retrievals using a vertical profile of temperature  
 and abundance estimated from Spitzer<sup>24</sup>, which has a lower CH<sub>4</sub> abundance of 3.2%, compared  
 with 4% for the ‘F1’ profile<sup>3</sup>, but is slightly warmer at pressures greater than 1 bar, resulting in  
 higher saturated vapour pressures of H<sub>2</sub>S. As might be expected, the lower CH<sub>4</sub> abundance of this  
 profile led to the retrieved cloud opacity peaking at slightly higher pressures to achieve the required  
 column abundance of CH<sub>4</sub> (Table 1) and the retrieved H<sub>2</sub>S relative humidity at the deeper cloud  
 tops in the warmer atmosphere was only  $16 \pm 2\%$ . Since it is not clear which of these two profiles is  
 more reliable, (although the ‘F1’ profile was found to be inconsistent with Spitzer observations<sup>24</sup>) it  
 can be seen that although we clearly detect the presence of H<sub>2</sub>S at Uranus’ cloud tops, it is difficult  
 to quantitatively determine its relative humidity. However, we can see from Table 1 that there is  
 very good correspondence between the retrieved values of column abundance of H<sub>2</sub>S above the  
 clouds for the two temperature profiles and also between the retrieved mole fraction of H<sub>2</sub>S at the  
 cloud-top pressure level of  $(4.7 \pm 0.5) \times 10^{-7}$  for the ‘F1’ profile and  $(4.3 \pm 0.5) \times 10^{-7}$  for the  
 Spitzer profile, where we have propagated the relative humidity retrieval errors.

Table 1 and Supplementary Figs. 3 – 11 show our fits at the other test points on Uranus’ disc,  
 indicated in Fig. 1. At all locations except in Uranus’ northern polar ‘cap’ feature we found a clear  
 improvement in our fit to the spectra when H<sub>2</sub>S absorption is included, indicating the presence of

H<sub>2</sub>S at the cloud tops (Table 1), with well defined column abundances of  $(2 - 5) \times 10^{19}$  molecule  
 cm<sup>-2</sup> and cloud-top mole fractions of 0.4 – 0.8 ppm. All but one of the chosen points were on the  
 central meridian, to keep the zenith angle as low as possible to minimise the computation time of  
 our multiple scattering code, which uses more Fourier components in the azimuth decomposition  
 direction as the zenith angle increases to maintain accuracy. However, point ‘2’ was chosen to be  
 at roughly the same latitude as our reference area, but off the central meridian and closer to the  
 limb to check that our retrieval was robust against zenith angle changes, which was found to be  
 the case. The absence of a clear H<sub>2</sub>S signature near Uranus’ north pole seems to indicate lower  
 H<sub>2</sub>S above the clouds in this region, in the same way that microwave observations found that the  
 polar regions were depleted in microwave absorbers (H<sub>2</sub>S and NH<sub>3</sub>) at depth<sup>6</sup>. The abundance of  
 methane above the clouds is also known to be reduced at these latitudes<sup>3,19</sup>. Alternatively, it could  
 also be that the H<sub>2</sub>S signal is masked by increased abundance of tropospheric haze, but Table 1,  
 which lists a haze ‘index’, given by the observed radiance in a methane absorbing band divided  
 by the radiance at continuum wavelengths, does not suggest that the polar region is particularly  
 affected by overlying haze. However, to explore this further requires a detailed examination of  
 spectra in the polar regions, which is beyond the scope of this paper.

If we could be sure that the main observed cloud deck was vertically thin and composed of  
 H<sub>2</sub>S ice, then we could constrain the abundance of H<sub>2</sub>S below it by equating the cloud base to  
 the condensation level. However, the low retrieved single-scattering albedo of the cloud particles  
 means that we cannot tell between whether we are seeing a vertically thin cloud based at 2–3 bar  
 or just the top of a vertically extended cloud that extends to several bars. Instead, our detection of

209 H<sub>2</sub>S can be used to give a lower limit on its abundance below the observed cloud. Assuming the  
 210 main cloud is made of H<sub>2</sub>S ice, is vertically thin and is based at 3 bars, and that the STIS/Voyager-  
 211 2 ‘F1’ temperature profile<sup>3</sup> we have assumed is correct, the saturated mole fraction of H<sub>2</sub>S at the  
 212 3-bar level (where the temperature is 116.1K) is estimated to be  $1.1 \times 10^{-5}$ . Alternatively, using  
 213 the Spitzer profile<sup>24</sup>, the saturated vapour mole fraction at the 3-bar level (where the temperature  
 214 is 119.5 K) is  $2.5 \times 10^{-5}$ . Hence, we can conclude that the mole fraction of H<sub>2</sub>S at pressures  
 215  $> 3$  bar, immediately below the clouds must be  $> (1.0 - 2.5) \times 10^{-5}$ . We can compare this  
 216 with the expected abundances of H<sub>2</sub>S and NH<sub>3</sub> from microwave VLA studies<sup>5-7</sup>, who found the  
 217 abundance of H<sub>2</sub>S to be  $10 - 30 \times$  solar, and  $S/N > \sim 5$ , assuming solar abundances<sup>8</sup> of H<sub>2</sub>S/H<sub>2</sub>  
 218  $= 3.76 \times 10^{-5}$  and  $NH_3/H_2 = 1.74 \times 10^{-4}$  (giving  $N/S = 4.6$ ). Using these values,  $10 \times$  solar H<sub>2</sub>S  
 219 and  $2 \times$  solar NH<sub>3</sub> would give a residual mole fraction of H<sub>2</sub>S above a deeper NH<sub>4</sub>SH cloud of at  
 220 least  $3 \times 10^{-5}$ , while for  $30 \times$  solar H<sub>2</sub>S and  $6 \times$  solar NH<sub>3</sub>, the expected residual H<sub>2</sub>S mole fraction  
 221 increases to  $9 \times 10^{-5}$ . Both these values are significantly greater than our estimated minimum  
 222 residual abundance, but are consistent with it and may suggest that the base of the cloud lies at  
 223 pressures greater than 3 bar. A more recent analysis of Spitzer Uranus observations<sup>24</sup> suggests a  
 224 residual H<sub>2</sub>S mole fraction of  $1.5 \times 10^{-5}$  in order to reconcile the millimetre spectrum with the  
 225 temperature profile derived from Spitzer, which is much closer to our estimate. Interpolating to  
 226 the pressure levels in our assumed ‘F1’ temperature-pressure profile<sup>3</sup> where the VLA and Spitzer  
 227 estimates of residual H<sub>2</sub>S abundance are equal to the saturated vapour pressure abundances we  
 228 deduce that the base of the main cloud must lie at a pressure of 3.1 – 4.1 bar. Alternatively, if  
 229 we assume the Spitzer temperature-pressure profile<sup>24</sup>, we find a pressure range 2.8 – 3.7 bar. The

fact that we detect  $\text{H}_2\text{S}$  at all at Uranus' cloud tops confirms that the deep abundance of  $\text{H}_2\text{S}$  must exceed that of  $\text{NH}_3$  and hence that  $\text{S/N} > 4.6 \times$  solar for the solar abundance ratios<sup>8</sup> assumed by the VLA study<sup>5,6</sup>. We note, however, that there are other, more recent estimates of the solar abundance ratios, for which the solar N/S value varies from 4.4<sup>25</sup> to 5.0<sup>26</sup>. Hence, to ensure that the deep abundance of  $\text{H}_2\text{S}$  exceeds that of  $\text{NH}_3$  we conclude that the S/N ratio in Uranus' bulk atmosphere exceeds  $4.4\text{--}5.0 \times$  solar. The clear detection of gaseous  $\text{H}_2\text{S}$  above Uranus' clouds leads us to conclude that  $\text{H}_2\text{S}$  ice likely forms a significant component of the main clouds at 1.2 – 3 bar. To our knowledge the imaginary refractive index spectrum of  $\text{H}_2\text{S}$  ice has not been measured and hence we cannot directly verify if our retrieved refractive index spectrum is consistent with  $\text{H}_2\text{S}$  ice. However, very large imaginary refractive indices, such as we retrieve, are absent in the measured complex refractive index spectra of  $\text{H}_2\text{O}$ ,  $\text{CH}_4$  and  $\text{NH}_3$  ices. This suggests that if Uranus' main clouds are indeed formed primarily of  $\text{H}_2\text{S}$  ice, the particles may not be pure condensates, but may be heavily coated or mixed with photochemical products drizzling down from the stratosphere above, lowering their single-scattering albedos.

## 1 References

1. de Kleer, K., Luszcz-Cook, S., de Pater, I., Ádámkovics, M., Hammel, H.B., 2015 Clouds and aerosols on Uranus: Radiative transfer modeling of spatially-resolved near-infrared Keck spectra. *Icarus* 256, 120 – 137.
2. Irwin, P.G.J., de Bergh, C., Courtin, R., Bézar, B., Teanby, N.A., Davis, G.R., Fletcher, L.N., Orton, G.S., Calcutt, S.B., Tice, D., Hurley, J., 2012b. The application of new methane

line absorption data to Gemini-N/NIFS and KPNO/FTS observations of Uranus' near-infrared spectrum. *Icarus* 220, 369 – 382.

3. Sromovsky, L.A., Fry, P.M., Kim, J.H., 2011. Methane on Uranus: The case for a compact CH<sub>4</sub> cloud layer at low latitudes and a severe CH<sub>4</sub> depletion at high latitudes based on a re-analysis of Voyager occultation measurements and STIS spectroscopy. *Icarus* 215, 292 – 312.

4. Weidenschilling, S.J., Lewis, J.S., 1973. Atmospheric and cloud structures of the Jovian planets. *Icarus* 20, 465 – 76.

5. de Pater, I., Romani, P.N., Atreya, S.K., 1991. Possible microwave absorption by H<sub>2</sub>S gas in Uranus' and Neptune's atmospheres. *Icarus* 91, 220 – 233.

6. de Pater, I., Romani, P.N., Atreya, S.K., 1989. Uranus' deep atmosphere revealed. *Icarus* 82, 288 – 313.

7. de Pater, I., Massie, S., 1985. Models of the millimeter-centimeter spectra of the giant planets. *Icarus* 62, 143 – 171.

8. Cameron, A.G.W., 1982. Elemental and Nuclidic Abundances in the Solar System. In *Essays in Nuclear Astrophysics* (C. A. Barnes, D. D. Clayton, and D. N. Schramm, Eds.), pp. 23-43, Cambridge Univ. Press, London/New York.

9. Niemann, H.B., et al., 1998. The composition of the jovian atmosphere as determined by the Galileo probe mass spectrometer. *J. Geophys. Res.* 103, 22831 – 22845.

- 270 10. Boissier, J., Bockelée-Morvan, Biver, N., Crovisier, J., Despois, D., Marsden, B.G., Moreno,  
271 R. 2007. Interferometric imaging of the sulfur-bearing molecules H<sub>2</sub>S, SO and CS in comet  
272 C/1995 O1 (Hale-Bopp). *Astron. Astrophys.* 475, 1131 – 1144.
- 273 11. Eberhardt, P., Meier, R., Krankowsky, D., Hodges, P.R., 1994. Methanol and hydrogen sulfide  
274 in comet P/Halley. *Astron. Astrophys.* 288, 315 – 329.
- 275 12. Noll, K.S., McGrath, M.A., Trafton, L.M., Atreya, S.K., Caldwell, J.J., Weaver, H.A., Yelle,  
276 R.V., Barnet, C., Edgington, S., 1995. HST Spectroscopic observations of Jupiter after the  
277 collision of Comet Shoemaker-Levy 9. *Science* 267, 1307 – 1313.
- 278 13. Lellouch, E., 1996. Chemistry induced by the impacts: Observations. IAU Colloquium 156;  
279 Proceedings of the Space Telescope Science Institute Workshop, held in Baltimore, Mary-  
280 land, May 9–12, 1995. Eds.: Keith S. Noll, Harold A. Weaver, Paul D. Feldman, Cambridge  
281 University Press, p. 213.
- 282 14. Irwin, P.G.J., Teanby, N.A., Davis, G.R., Fletcher, L.N., Orton, G.S., Tice, D., Kyffin, A.,  
283 2011. Uranus’ cloud structure and seasonal variability from Gemini-North and UKIRT obser-  
284 vations. *Icarus* 212, 339 – 350.
- 285 15. Irwin, P.G.J., Teanby, N.A., Davis, G.R., Fletcher, L.N., Orton, G.S., Calcutt, S.B., Tice, D.,  
286 Hurley, J., 2012. Further seasonal changes in Uranus’ cloud structure observed by Gemini-  
287 North and UKIRT. *Icarus* 218, 47 – 55.

16. Irwin, P.G.J., Teanby, N.A., de Kok, R., Fletcher, L.N., Howett, C.J.A., Tsang, C.C.C., Wilson, C.F., Calcutt, S.B., Nixon, C.A., Parrish, P.D., 2008. The NEMESIS planetary atmosphere radiative transfer and retrieval tool. *J.Q.S.R.T.* 109, 1136 – 1150.
17. Campargue, A., Leshchishina, O., Wang, L., Mondelain, D., Kass, S., 2013. The WKLMC empirical line lists (5852 – 7919  $\text{cm}^{-1}$ ) for methane between 80 K and 296 K: “Final” lists for atmospheric and planetary applications. *J. Molec. Spectrosc.* 291, 16 – 22.
18. Rothman, L.S., Gordon, I.E., Babikov, Y., Barbe, A., Benner, D.C., Bernath, P.F., et al, 2013. The HITRAN2012 molecular spectroscopic database, *J.Q.S.R.T.* 130, 4 – 50.
19. Karkoschka, E., Tomasko, M., 2009. The haze and methane distributions on Uranus from HST-STIS spectroscopy. *Icarus* 202, 287–309.
20. Fray, N., Schmitt, B., 2009. Sublimation of ices of astrophysical interest: A bibliographic review. *Plan. Space. Sci.* 57, 2053 – 2080.
21. Irwin, P.G.J., Tice, D.S., Fletcher, L.N., Barstow, J.K., Teanby, N.A., Orton, G.S., Davis, G.R., 2015. Reanalysis of Uranus’ cloud scattering properties from IRTF/SpeX observations using a self-consistent scattering cloud retrieval scheme. *Icarus* 250, 462 – 476.
22. Karkoschka, E., Tomasko, M., 2010. Methane absorption coefficients for the jovian planets from laboratory, Huygens, and HST data. *Icarus* 205, 674 – 694.
23. Sromovsky, L.A., Fry, P.M., 2007. Spatially resolved cloud structure on Uranus: Implications of near-IR adaptive optics imaging. *Icarus* 192, 527 – 557.



24. Orton, G.S., Fletcher, L.N., Moses, J.I., Mainzer, A., Hines, D., Hammel, H., Martin-Torres, J., Burgdorf, M., Merlet, C., Line, M.R., 2014. 1. Mid-Infrared spectroscopy of Uranus from the Spitzer Infrared Spectrometer: Determination of the mean temperature of the upper troposphere and stratosphere. *Icarus* 243, 494 – 513.
25. Grevesse, N., Asplund, M., Sauval, A.D., 2007. The solar chemical composition. *Space Sci. Rev.* 130, 105 – 114.
26. Lodders, K., 2010. Solar System Abundances of the Elements, in *Principles and Perspectives in Cosmochemistry, Astrophysics and Space Science Proceedings*, ISBN 978-3-642-10351-3. Springer-Verlag Berlin Heidelberg, p. 379.

**Correspondence** Correspondence and requests for materials should be addressed to Patrick G. J. Irwin (email: [patrick.irwin@physics.ox.ac.uk](mailto:patrick.irwin@physics.ox.ac.uk)).

**Acknowledgements** We are grateful to the United Kingdom Science and Technology Facilities Council for funding this research and also to our support astronomers: Richard McDermid and Chad Trujillo (2009, 2010). The Gemini Observatory is operated by the Association of Universities for Research in Astronomy, Inc., under a cooperative agreement with the NSF on behalf of the Gemini partnership: the National Science Foundation (United States), the Science and Technology Facilities Council (United Kingdom), the National Research Council (Canada), CONICYT (Chile), the Australian Research Council (Australia), Ministério da Ciência e Tecnologia (Brazil) and Ministerio de Ciencia, Tecnología e Innovación Productiva (Argentina). We thank Larry Sromovsky for providing the code used to generate our Rayleigh-scattering opacities. Glenn Orton was supported by NASA funding to the Jet Propulsion Laboratory, California Institute of Technology.

Leigh Fletcher was supported by a Royal Society Research Fellowship at the University of Leicester.

**Author Contributions** P.G.J.I. wrote the proposal to make the original observations and reduced the data and re-analysed it using the NEMESIS code; B.B. and R.G. assisted in identifying and validating the line data used. G.A.O. provided the Spitzer T-P profile used. L.N.F., N.A.T., D.T., and all co-authors contributed to the analysis, interpretation of the results, and all co-wrote the final paper.

**Competing Interests** The authors declare that they have no competing financial interests.

## 2 Figure Legends

Figure 1. Panel A: The appearance of Uranus at  $1.55 \mu\text{m}$ , observed with Gemini/NIFS on 2nd November 2010 at approximately 06:00UT, showing the position of the seven  $5 \times 5$  pixel test areas picked for retrieval analysis. Panel B: The appearance of Uranus at  $1.62 \mu\text{m}$ . Panel C: Reference spectrum of Uranus<sup>14</sup> analysed in this study, averaged over area ‘1’ just north of the equator, near the disc centre, with a mean latitude of  $15.3^\circ\text{N}$ , and error estimates shown in grey. Panel D: Mean strength listed in the k-distribution tables used in this study across the Gemini/NIFS spectral range. These absorption tables were generated from the WKLMC@80K+<sup>17</sup> database for  $\text{CH}_4$ , and from HITRAN2012<sup>18</sup> for  $\text{H}_2\text{S}$  and  $\text{NH}_3$ . These mean absorption coefficients have been computed at a temperature of 100 K and pressure of 1 atm, similar to conditions found at the tops of Uranus’ main visible clouds. Note that for  $\text{NH}_3$ , the linedata in HITRAN2012 terminate at  $1.587 \mu\text{m}$ , roughly half way through the  $\text{H}_2\text{S}$  absorption band.

Figure 2. Assumed pressure variation of temperature (left-hand panel) and condensible abun-

dance (right-hand panel) assumed in this study for Uranus. The temperature-pressure profile is based on the ‘F1’ profile<sup>3</sup>. The vertical variation of the CH<sub>4</sub> abundance is as described in the text. The abundances of NH<sub>3</sub> and H<sub>2</sub>S have simply been limited by their saturation vapour pressures.

Figure 3. Fits to average Gemini/NIFS observation of Uranus, made on 2nd November 2010 at 15.3° N, using three different assumptions for the *a priori* imaginary refractive index spectrum, and excluding H<sub>2</sub>S and NH<sub>3</sub> absorption. The red line shows the results using  $n_i = 0.001 \pm 0.0005$ , the black line shows the results using  $n_i = 0.01 \pm 0.005$ , while the blue lines show the results using  $n_i = 0.1 \pm 0.05$ . Panel a) shows the fits to the measured spectra, panel b) shows the difference between the observed and modelled spectra. Panel c) shows the fitted imaginary refractive index spectra of the one type of particle assumed right hand plot, while panel d) shows the fitted cloud profiles (opacity/bar at 1.6  $\mu\text{m}$ ). In panels c) and d) the *a priori* value and range is marked in light grey, while the error range on the retrieved quantities is indicated in darker grey. The  $\chi^2/n$  of the fits is also shown in panel a).

Figure 4. Fits to the co-added Gemini/NIFS observation of Uranus in the wavelength range 1.56 – 1.6  $\mu\text{m}$ . In the top plot, the observed reflectivity spectrum and estimated error is shown in grey. The fitted spectrum when H<sub>2</sub>S absorption is not included is shown in red, while the fitted spectrum when H<sub>2</sub>S absorption is included is shown in black. The bottom plot shows the differences between these fits and the observed spectrum using the same colours (i.e. red when H<sub>2</sub>S absorption is not included and black when it is), with the error range again shown in grey. The blue line in the bottom plot shows how the calculated spectrum for the fit when H<sub>2</sub>S absorption is

not included (i.e. red line in the top plot) changes when H<sub>2</sub>S absorption is added (leaving all other fitted parameters unchanged), assuming a profile with 100% relative humidity (RH). The cyan line shows how the calculated spectrum changes when NH<sub>3</sub> absorption is added, leaving all other fitted parameters unchanged, assuming a profile with 1000 times the *a priori* NH<sub>3</sub> profile with 100% RH.

## Methods

**Spectral Data Sources** The main gaseous absorber in the H-band (1.4 – 1.8  $\mu\text{m}$ ) in Uranus’ spectrum is methane. The best available source of methane line data at low temperature in this range is the WKLMC@80K<sup>+17</sup> line database, which contains the positions, strengths, lower-state energies and empirical estimates of the rotational quantum number  $J$ , of lines measured at 80K and 296K. These lines are improved over the WKMC@80<sup>27</sup> database, previously used to analyse the Gemini/NIFS observations reanalysed here for Uranus<sup>2</sup> as they include extra lines that were detected at 296K, but not at 80K, and we have further improved our assignment of line widths, as described below. For the lines detected at 296K, but not 80K, lower state energies were defined so as to yield an intensity at 80 K just below the measurement sensitivity threshold. Hence, the contribution of these lines at cold temperatures bears significant uncertainty. For the lines detected at 80K, but not 296 K, the lower state energies were arbitrarily set to  $-1.0 \text{ cm}^{-1}$ . These line data were converted to HITRAN format, using the listed strengths at 296 K directly for lines observed at both 80 K and 296 K, and for lines observed only at 80K, we extrapolated their strengths to 296 K using the listed arbitrary lower state energy of  $-1.0 \text{ cm}^{-1}$  and total partition function (rotational + vibrational)

386 provided as part of HITRAN2012<sup>18</sup>. The spectral range covered by these data is 5852 – 7919  
 387  $\text{cm}^{-1}$  (1.262 – 1.709  $\mu\text{m}$ ). These measurements were made for “natural” methane gas, for which  
 388 the  $\text{CH}_3\text{D}/\text{CH}_4$  ratio is estimated<sup>17</sup> to be  $5 \times 10^{-4}$ . This is not suitable for calculations in Uranus’  
 389 atmosphere, for which the most precise estimate<sup>28</sup> of  $\text{CH}_3\text{D}/\text{CH}_4$  is  $(2.96^{+0.71}_{-0.64}) \times 10^{-4}$  (using an  
 390 isotopic enrichment factor<sup>29</sup> of  $f = 1.68 \pm 0.23$ ). Hence, lines for  $\text{CH}_3\text{D}$  were scaled in strength  
 391 by 2.96/5. For the foreign-broadened line widths, we used  $J$ -dependent  $\text{H}_2$ - and He-broadened  
 392 widths<sup>30</sup>, to which we fitted a 4th-order polynomial in  $J$ , using the widths calculated for  $J = 13$   
 393 for higher values of  $J$  to prevent inaccurate extrapolation<sup>31,32</sup>. We assumed temperature depen-  
 394 dence coefficients of these foreign-broadened widths for  $\text{H}_2$ -broadening<sup>33</sup> and He-broadening<sup>35</sup>.  
 395 For the line shape, we used a Voigt function, but with sub-Lorentzian correction far from line cen-  
 396 tre as recommended for  $\text{H}_2$ -broadening conditions<sup>36</sup>. However, we also tested the sub-Lorentzian  
 397 corrections suggested for Titan spectra<sup>37</sup> and a sub-Lorentzian correction previously suggested for  
 398 modelling Uranus spectra<sup>38</sup>. Using these three different line shapes we took account of all lines  
 399 within  $250 \text{ cm}^{-1}$  of each calculation wavelength.

400 Spectroscopic line data for hydrogen sulphide ( $\text{H}_2\text{S}$ ) and ammonia ( $\text{NH}_3$ ) were taken from  
 401 HITRAN2012<sup>18</sup>. The line widths and their temperature exponents were also taken from the foreign-  
 402 broadened data listed in HITRAN2012. For  $\text{H}_2\text{S}$  these are  $\gamma_{air} = 0.074 \text{ cm}^{-1} \text{ atm}^{-1}$  and a tem-  
 403 perature exponent of 0.75, for all lines. HITRAN2012 note that detailed laboratory investigations  
 404 are needed to characterise how the line widths vary with the ro-vibrational quantum number, and  
 405 there appears to be no published evidence on the appropriate values for an  $\text{H}_2/\text{He}$ -broadening  
 406 atmosphere. Similarly, for  $\text{NH}_3$ , we used the published HITRAN2012 foreign-broadening param-

eters. If the absorption of  $\text{NH}_3$  had proved to be significant, we might have attempted to use line-broadening parameters more suited to  $\text{H}_2/\text{He}$ -broadening conditions. However, as reported in our paper, the absorption of  $\text{NH}_3$  was not detected in these observations and hence there was no error introduced by using the listed HITRAN2012 air-broadened widths. We also examined using ExoMOL line data for  $\text{H}_2\text{S}$ <sup>39</sup> and found negligible differences in the spectra computed at Gemini/NIFS resolution with the HITRAN2012 line data. Since the HITRAN2012 line data are much easier to handle (they contain far fewer ‘hot lines’, which are only relevant for high-temperature calculations) and probably have better constrained line frequencies, we decided to use HITRAN2012 for both  $\text{NH}_3$  and  $\text{H}_2\text{S}$  line data. In both cases, in the absence of any better information and in the expectation of weak absorptions (for which the exact line widths are less important), we used the published HITRAN2012 air-broadened widths and a Voigt line shape, with a line wing cut-off of  $35 \text{ cm}^{-1}$  to account for typical sub-Lorentzian wing corrections.

The line data were converted to k-distribution look-up tables, or k-tables, covering the Gemini/NIFS H-band spectral range, with 20 g-ordinates, 15 pressures, equally spaced in log pressure between  $10^{-4}$  and 10 bar, and 14 temperatures, equally spaced between 50 and 180 K. These tables were precomputed with the modelled instrument line shape of the Gemini/NIFS observations, set to be Gaussian with a full-width-half-maximum (FWHM) of  $0.0003 \mu\text{m}$ , after an analysis of ARC lamp calibration spectra<sup>2</sup>.

**Observations and wavelength calibration** Observations of Uranus were made with Gemini-North’s Near-infrared Integral Field Spectrometer (NIFS) instrument in September 2009 and October/November 2010<sup>14, 15</sup>, with adaptive optics using Uranus’ nearby moons for wavefront sensing

(e.g. Ariel, Titania). NIFS' H-band spectral resolution gives a Gaussian instrument function with spectral resolution of  $\text{FWHM} = 0.0003 \mu\text{m}$ . The wavelength calibration provided by the standard pipeline of Gemini/NIFS was found to be not quite accurate enough to match the spectral features observed here. The assumed wavelength of sample  $i$  in the spectrum is set to  $\lambda_i = \lambda_0 + (i - i_0)\lambda_1$ , where  $i_0$  is the sample number of the 'central' wavelength, and the wavelength centre and step were initially assumed to be  $\lambda_0 = 1.55 \mu\text{m}$  and  $\lambda_1 = 0.000155 \mu\text{m}$ , respectively. By comparing the measured spectrum to our initial fitted spectrum we found that we could achieve a much better fit by modifying these values to  $\lambda_0 = 1.54995 \mu\text{m}$  and  $\lambda_1 = 0.00016036 \mu\text{m}$ . We used these values in the subsequent analysis.

**Uranus vertical profiles of temperature and gaseous abundance** The reference temperature and abundance profile used in this study (Fig. 2) is based on the 'F1' STIS/Voyager-2 profile<sup>3</sup>. This profile has a deep methane mole fraction of 4%<sup>19</sup>, and has a varying relative humidity with height above the condensation level. The He:H<sub>2</sub> ratio in this profile is set to 0.131 and the profile includes 0.04% mole fraction of Ne. To this profile we added abundance profiles of NH<sub>3</sub> and H<sub>2</sub>S, assuming arbitrary 'deep' mole fractions (i.e. above the putative NH<sub>4</sub>SH cloud) of 0.001 for both, and limited their abundance to not exceed the saturated vapour pressure in the troposphere as the temperature falls with height. As the abundances of these gases (and CH<sub>4</sub>) decrease with pressure the abundance of H<sub>2</sub> and He is adjusted to ensure the sum of mole fractions adds to unity (keeping He:H<sub>2</sub> = 0.131, or equivalently 12:88); the heights are calculated from the hydrostatic equation using the local temperature, gravitational acceleration and local mean total molecular weight.

For comparison we also performed retrievals using the temperature-pressure profile deter-

449 mined by from Spitzer observations of Uranus' mid-IR spectrum<sup>24</sup>, again with 'deep' NH<sub>3</sub> and  
450 H<sub>2</sub>S abundances of 0.001. H<sub>2</sub> and He were assumed to be present with a ratio 85:15, again ensur-  
451 ing the sum of mole fractions adds to unity at all heights.

452 **Radiative-transfer analysis** The vertical cloud structure was retrieved from the Gemini/NIFS ob-  
453 servations using the NEMESIS<sup>16</sup> radiative-transfer and retrieval code. NEMESIS models planetary  
454 spectra either using a line-by-line model, or by using the correlated-k approximation<sup>40</sup>. For speed,  
455 these retrievals were conducted using the method of correlated-k, but we regularly checked that  
456 we obtained the same model spectra (to within error) using a line-by-line approach. To model  
457 these reflected-sunlight spectra, a matrix-operator multiple-scattering model<sup>41</sup> was used, with 5  
458 zenith angles (upwards and downwards, respectively) and the number of required components in  
459 the Fourier azimuth decomposition determined from the maximum of the reflected or incident-  
460 solar zenith angles. The collision-induced absorption of H<sub>2</sub>-H<sub>2</sub> and H<sub>2</sub>-He was modelled with  
461 published coefficients<sup>42-44</sup>. Rayleigh scattering was also included for completeness, but was found  
462 to be negligible at these wavelengths.

463 To analyse the measured radiance spectra within our radiative transfer model we initially  
464 used the high-resolution 'CAVIAR' solar spectrum<sup>45</sup>, which we smoothed to the NIFS resolution of  
465  $\Delta\lambda = 0.0003\mu\text{m}$ . However, we found that this spectrum (and others, e.g.<sup>46,47</sup>) contained spurious  
466 'Fraunhofer lines' that did not seem to correspond to features seen at these wavelengths in the  
467 Uranus spectra. We must assume that the method used to generate these 'Extraterrestrial Solar  
468 Spectra' (ESS), namely measuring the solar spectrum at the ground at various zenith angles and  
469 extrapolating to an airmass of zero, leads to small errors at these wavelengths. Hence, we used



470 a smoothed version of the solar spectrum<sup>47</sup> in our calculations, omitting the spurious ‘Fraunhofer  
471 lines’, which we found matched our observations much more closely.

472 The observed spectrum (with  $n_y = 937$  spectral points) was fitted with NEMESIS using a  
473 continuous distribution of cloud particles whose opacity at 39 levels spaced between  $\sim 10$  and  
474  $\sim 0.01$  bar was retrieved. For this cloud profile the *a priori* opacity values (at  $1.6 \mu\text{m}$ ) were set to  
475  $0.001 \pm 0.0005 \text{ g}^{-1} \text{ cm}^2$  at all levels (equating to opacity/bar values of  $\sim 1$ ), with a ‘correlation  
476 length’ of 1.5 scale heights to ensure the profile was vertically smooth. NEMESIS treats cloud  
477 opacity as log values and so the error was converted to  $\pm 50\%$ . The particles were assumed to  
478 have a standard Gamma size distribution with mean radius  $1.0 \mu\text{m}$  and variance 0.05, which are  
479 typical values assumed in previous analyses. Using a previously published technique<sup>21</sup>, the imag-  
480 inary refractive index of these particles was set to 1.4 at a wavelength of  $1.6 \mu\text{m}$  and NEMESIS  
481 used to retrieve the imaginary refractive index spectrum. The *a priori* imaginary refractive index  
482 spectrum was sampled at every  $0.05 \mu\text{m}$  between  $1.4$  and  $1.8 \mu\text{m}$ , with a ‘correlation length’ of  
483  $0.1 \mu\text{m}$  set in the covariance matrix, to ensure that retrieved spectrum varied reasonably smoothly  
484 with wavelength. Hence there were  $n_x = 48$  free variables in our retrieval setup. At each iter-  
485 ation of the model, the real part of the particles’ refractive index spectrum was computed using  
486 the Kramers-Kronig relation<sup>48</sup>. Self-consistent scattering properties were then calculated using  
487 Mie theory, but the Mie-calculated phase functions were approximated with combined Henyey-  
488 Greenstein functions at each wavelength to smooth-over features peculiar to perfectly spherical  
489 scatterers such as the ‘rainbow’ and ‘glory’. This is justified since we expect the actual aerosols  
490 in the atmosphere of Uranus to be solid condensates, and thus non-spherical. However, assuming

these non-spherical particles are randomly orientated with respect to each other, the bulk scattering properties, such as cross-section and single-scattering albedo, are reasonably approximated with Mie theory<sup>34</sup>, especially if the phase functions are also modified as we describe.

Since methane is the main gaseous absorber we tested to see whether some of the approximations assumed in the WKLMC@80K+<sup>17</sup> line database might be having an adverse effect on our calculations. We first checked whether excluding the lines observed at 296 K, but not at 80 K (and which are assigned a lower state energy high enough to reduce the computed strength at 80 K to be below the measurement noise limit) might significantly affect the calculated spectra, but found very little difference when these lines were neglected. We also checked the effect excluding the lines observed only at 80 K as well (and which are assigned an arbitrary lower state energy of 1  $\text{cm}^{-1}$ ). In this case, the differences were larger, but on the whole the model correctly reproduced the shape and main features of the observed spectrum.

**Retrieval Tests** Supplementary Fig. 12 shows our fit to the Uranus spectrum, setting the *a priori* imaginary refractive indices to  $0.01 \pm 0.005$  at all wavelengths and using the three different sub-Lorentzian line shapes for  $\text{CH}_4$  (neglecting  $\text{H}_2\text{S}$  and  $\text{NH}_3$  absorption). We found that each assumption for the sub-Lorentzian correction gave a very similar fit to the spectrum ( $\chi^2/n \sim 1.7\text{--}1.9$ ), which was initially puzzling. However, the reason for this is easy to understand from Supplementary Fig. 12. The effect of different sub-Lorentzian corrections is most apparent on the shortwave side of the strong absorption band at  $1.7 - 1.8 \mu\text{m}$  and previous studies have tuned the correction to get the best match to the observed spectrum between  $1.5$  and  $1.62 \mu\text{m}$ . Our current model, however, can very easily fit this region by varying the imaginary refractive index spectrum

512 of the particles and it can be seen that very different imaginary refractive index spectra are retrieved  
 513 for the three different sub-Lorentzian corrections, but very similar vertical cloud distributions and  
 514 similar spectral fits. In other words, there is a degeneracy between the sub-Lorentzian corrections  
 515 and the retrieved imaginary refractive index. In fact, we had to be careful not to allow the imagi-  
 516 nary refractive index retrieval too much freedom. Early retrievals sampled the imaginary refractive  
 517 index spectrum more finely ( $\Delta\lambda = 0.005\mu\text{m}$ ) over the  $1.56 - 1.6\mu\text{m}$  range and significant part  
 518 of the spectral variation of reflectivity was accounted for by variations in  $n_i$ , which it was difficult  
 519 to justify as being realistic. We thus assumed the slow wavelength-to-wavelength variation in  $n_i$   
 520 as described. Since the line shape recommended for  $\text{H}_2\text{-He}$  atmospheres<sup>36</sup> gave a good fit to the  
 521 observations, we chose to use this assumption in our final analysis.

522 **Scattering Properties** Since the fitted imaginary refractive index spectrum for our cloud particles  
 523 has values of typically  $n_i \sim 0.06$ , this leads the particles to be quite absorbing. This can best be  
 524 seen in Supplementary Fig. 1, where we compare the computed wavelength dependence of the  
 525 extinction cross-section (normalised to  $1.6\mu\text{m}$ ), the single-scattering albedo, and the asymmetry,  
 526  $g$ , of the forward part of the fitted combined Henyey-Greenstein phase functions for the case when  
 527 the *a priori* imaginary refractive indices were set to  $0.01 \pm 0.005$ . We found the back-scattering  
 528 part of the phase-function to be insignificant. As we can see the single-scattering albedo has values  
 529 of  $\varpi = 0.7 - 0.8$ , while the phase function asymmetry,  $g$ , is  $\sim 0.7$ .

### 3 Data availability statement

The data that support the plots within this paper and other findings of this study are available from the corresponding author upon reasonable request.

### 4 Methods References

27. Campargue, A., Wang, L., Mondelain, D., Kassi, S., Bézard, B., Lellouch, E., Coustenis, A., de Bergh, C., Hirtzig, M., Drossart, P., 2012. An empirical line list for methane in the 1.26 – 1.71  $\mu\text{m}$  region for planetary investigations ( $T = 80 - 300 \text{ K}$ ). Application to Titan. *Icarus* 219, 110 – 128.
28. Feuchtgruber, H., Lellouch, E., Orton, G., de Graauw, T., Vandenbussche, B., Swinyard, B., Moreno, R., Jarchow, C., Billebaud, F., Cavalié, T., Sidher, S., Hartogh, P., 2013. The D/H ratio in the atmospheres of Uranus and Neptune from Herschel-PACS observations. *Astron. Astrophys.* 551, A126.
29. Lécluse, C., Robert, F., Gautier, D., Guiraud, M. 1996. Deuterium enrichment in giant planets. *Planet. Space Sci.* 44, 1579 – 1592.
30. Pine A. S., 1992. Self-,  $\text{N}_2$ -,  $\text{O}_2$ -,  $\text{H}_2$ -, Ar-, and He- broadening in the  $\nu_3$  band Q branch of  $\text{CH}_4$ . *Journal of Chemical Physics* 97, 773 – 785.
31. Amundsen D. S., Baraffe I., Tremblin P., Manners J., Hayek W., Mayne N. J., Acreman D. M., 2014. Accuracy tests of radiation schemes used in hot Jupiter global circulation models,

Astron. Astrophys. 564, A59.

32. Garland, R., Irwin, P.G.J., 2017. Effectively calculating gaseous absorption in radiative transfer models of exoplanetary and brown dwarf atmospheres, Mon. Not. R. Astro. Soc.. (in preparation).

33. MargoIis J. S., 1993. Hydrogen broadening and collision-induced line shifts of methane at  $4200\text{ cm}^{-1}$ . J.Q.S.R.T. 49, 71 – 79.

34. Mishchenko M. I., Travis, L. D., Khan, R.A., West, R. A., 1997. Modeling phase functions for dustlike tropospheric aerosols using a shape mixture of randomly oriented polydisperse spheroids. J. Geophys. Res., 102, 16831 – 16847.

35. Varanasi P., Chudamani S., 1990. The temperature dependence of lineshifts, linewidths and line intensities of methane at low temperatures. J.Q.S.R.T. 43, 1 – 11.

36. Hartmann, J.-M., Boulet, C., Brodbeck, C., van Thanh, N., Fouchet, T., Drossart, P., 2002. A far wing lineshape for H<sub>2</sub> broadened CH<sub>4</sub> infrared transitions. J.Q.S.R.T. 72, 117 – 122.

37. de Bergh, C., Courtin, R., Bézard, B., Coustenis, A., Lellouch, E., Hirtzig, M., Rannou, P., Drossart, P., Campargue, A., Kass, S., Wang, L., Boudon, V., Nikitin, A., Tyuterev, V., 2012. Applications of a new set of methane line parameters to the modeling of Titan's spectrum in the  $1.58\text{ }\mu\text{m}$  window. Planet. Space Sci. 61, 85 – 98.

38. L.A. Sromovsky, Fry, P.M., Boudon, V., Campargue, A., Nikitin, A., 2012. Comparison of line-by-line and band models of near-IR methane absorption applied to outer planet atmospheres. Icarus 218, 1 – 23.

39. Azzam, A. A. A., Tennyson, J., Yurchenko, S. N., Naumenko, O. V., 2016. ExoMol molecular line lists - XVI: The rotation-vibration spectrum of hot H<sub>2</sub>S. M.N.R.A.S. 460, 4063 – 4074.
40. Lacis, A.A., Oinas, V., 1991. A description of the correlated-k distribution method for modelling nongray gaseous absorption, thermal emission, and multiple scattering in vertically inhomogeneous atmospheres. J.Geophys.Res. 96, 9027 – 9063.
41. Plass, G.N., Kattawar, G.W., Catchings, F.E., 1973. Matrix operator method of radiative transfer. 1: Rayleigh scattering. Appl. Opt. 12, 314 – 329.
42. Borysow, A., 1991. Modeling of collision-induced infrared absorption spectra of H<sub>2</sub> – H<sub>2</sub> pairs in the fundamental band at temperatures from 20 to 300 K. Icarus 92, 273 – 279.
43. Borysow, A., 1992. New model of collision-induced infrared absorption spectra of H<sub>2</sub> – He pairs in the 2 – 2.5  $\mu$ m range at temperatures from 20 to 300 K – An update. Icarus 96, 169 – 175.
44. Zheng, C., Borysow, A., 1995. Modeling of collision-induced infrared absorption spectra of H<sub>2</sub> pairs in the first overtone band at temperatures from 20 to 500 K. Icarus 113, 84 – 90.
45. Menang, K.P., Coleman, M.D., Gardiner, T.D., Ptashnik, I.V., Shine, K.P., 2013. A high-resolution near-infrared extraterrestrial solar spectrum derived from ground-based Fourier transform spectrometer measurements. J.Geophys.Res. 118, 5319 – 5331.
46. Fiorenza, C., Formisano, V., 2005. A solar spectrum for PFS data analysis. Planet. Space Sci. 53, 1009 – 1016.

- 588 47. Thuillier, G., Hersé, M., Labs, D., Foujols, T., Peetermans, W., Gillotay, D., Simon, P.C.,  
589 Mandel, H., 2003. The solar spectral irradiance from 200 to 2400 nm as measured by the  
590 SOLSPEC spectrometer from the ATLAS and EURECA missions, *Solar Physics* 214, 1 – 22.
- 591 48. Sheik-Bahae, M., 2005. Nonlinear Optics Basics. Kramers-Kronig Relations in Nonlinear  
592 Optics. In Robert D. Guenther. *Encyclopedia of Modern Optics*. Amsterdam: Academic Press.

Table 1: Retrieval results at all areas considered on Uranus' disc.

Area	Latitude	$p_1$	$f_{H_2S}$	$\chi^2/n$	$\chi^2/n_y$	$\Delta\chi^2$	$x_{H_2S}$	$A_{H_2S}$	$R_H$
1 <sup>a</sup>	15.3°N	1.99	113 ± 12	1.30	1.23	367.3	0.47	2.7	2.1
2	13.8°N	2.00	134 ± 19	1.04	0.99	140.7	0.58	3.3	2.3
3	15.3°S	2.10	123 ± 16	1.23	1.17	225.1	0.80	4.9	2.5
4	32.5°N	1.88	303 ± 45	1.31	1.24	218.7	0.82	4.4	2.6
5	44.7°N	1.66	474 ± 84	1.33	1.26	172.9	0.43	2.1	2.8
6 <sup>b</sup>	62.0°N	1.56	252 ± 211	1.31	1.24	1.8	0.13	0.6	3.9
7	4.9°N	1.98	96 ± 9	1.57	1.48	333.8	0.38	2.2	2.2
1 <sup>c</sup>	15.3°N	2.28	16 ± 2	1.36	1.29	292.1	0.43	2.9	2.1

Notes:  $p_1$  is the pressure(bar) where the cloud opacity to space is unity;  $f_{H_2S}$  is the retrieved H<sub>2</sub>S relative humidity (%);  $\chi^2/n$  is the reduced chi-squared statistic of the fit when H<sub>2</sub>S is included, where  $n = n_y - n_x = 889$ ;  $\chi^2/n_y$  is the chi-squared statistic of the fit when H<sub>2</sub>S is included, where  $n_y = 937$ ;  $x_{H_2S}$  is mole fraction of H<sub>2</sub>S (ppm) at  $p_1$ ;  $A_{H_2S}$  is the column amount of H<sub>2</sub>S ( $10^{19}$  molecule cm<sup>-2</sup>) above  $p_1$ ;  $R_H$  is a haze 'index' – the ratio of the average radiance from 1.63 – 1.64  $\mu$ m divided by the average radiance from 1.57 – 1.58  $\mu$ m, expressed as %.

Further notes: <sup>a</sup>Area 1 is the main area studied; <sup>b</sup>For polar area 6, where the radiance is lower, the measurement errors did not need to be multiplied by 1.6 ensure a good  $\chi^2/n$ ; <sup>c</sup>Same area as reference, but analysed using the Spitzer temperature profile, rather than 'F1'.



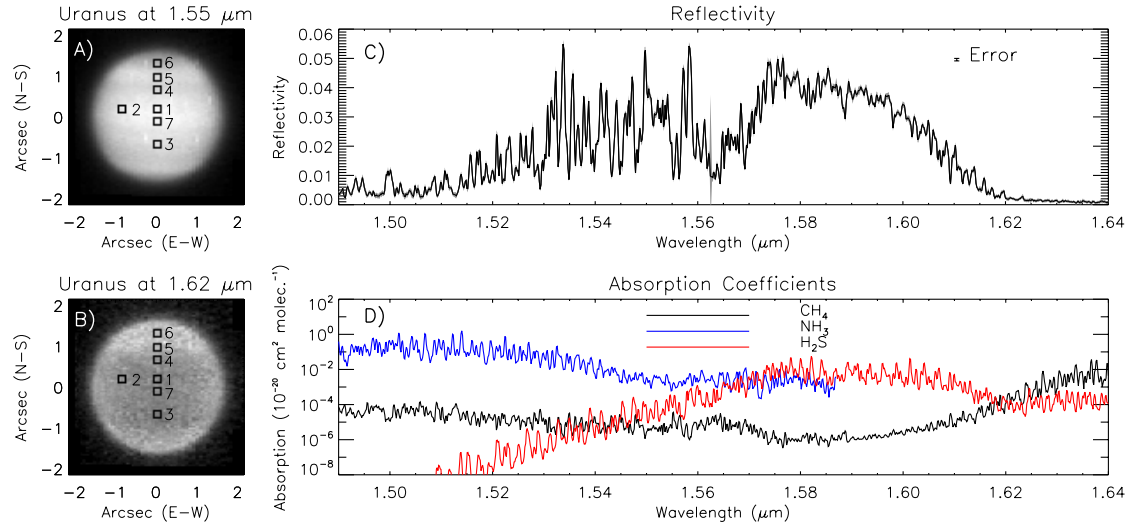


Figure 1: Panel A: The appearance of Uranus at 1.55  $\mu\text{m}$ , observed with Gemini/NIFS on 2nd November 2010 at approximately 06:00UT, showing the position of the seven  $5 \times 5$  pixel test areas picked for retrieval analysis. Panel B: The appearance of Uranus at 1.62  $\mu\text{m}$ . Panel C: Reference spectrum of Uranus<sup>14</sup> analysed in this study, averaged over area ‘1’ just north of the equator, near the disc centre, with a mean latitude of 15.3°N, and error estimates shown in grey. Panel D: Mean strength listed in the k-distribution tables used in this study across the Gemini/NIFS spectral range. These absorption tables were generated from the WKLMC@80K+<sup>17</sup> database for  $\text{CH}_4$ , and from HITRAN2012<sup>18</sup> for  $\text{H}_2\text{S}$  and  $\text{NH}_3$ . These mean absorption coefficients have been computed at a temperature of 100 K and pressure of 1 atm, similar to conditions found at the tops of Uranus’ main visible clouds. Note that for  $\text{NH}_3$ , the linedata in HITRAN2012 terminate at 1.587  $\mu\text{m}$ , roughly half way through the  $\text{H}_2\text{S}$  absorption band.

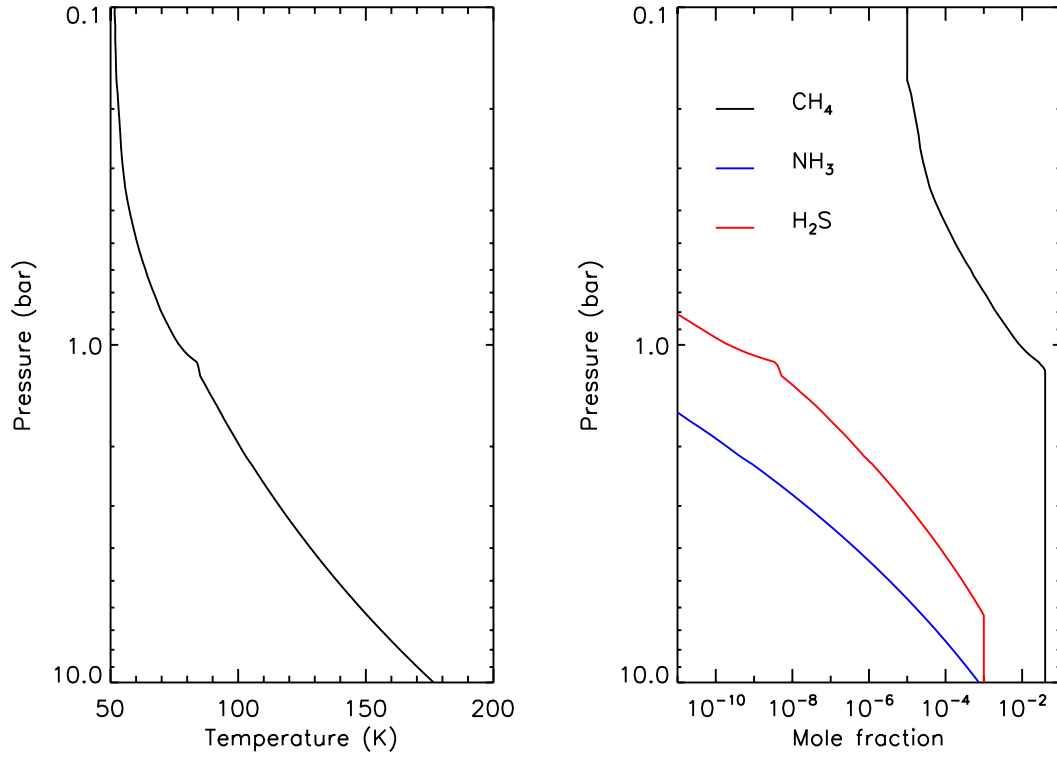


Figure 2: Assumed pressure variation of temperature (left-hand panel) and condensible abundance (right-hand panel) assumed in this study for Uranus. The temperature-pressure profile is based on the ‘F1’ profile<sup>3</sup>. The vertical variation of the CH<sub>4</sub> abundance is as described in the text. The abundances of NH<sub>3</sub> and H<sub>2</sub>S have simply been limited by their saturation vapour pressures.

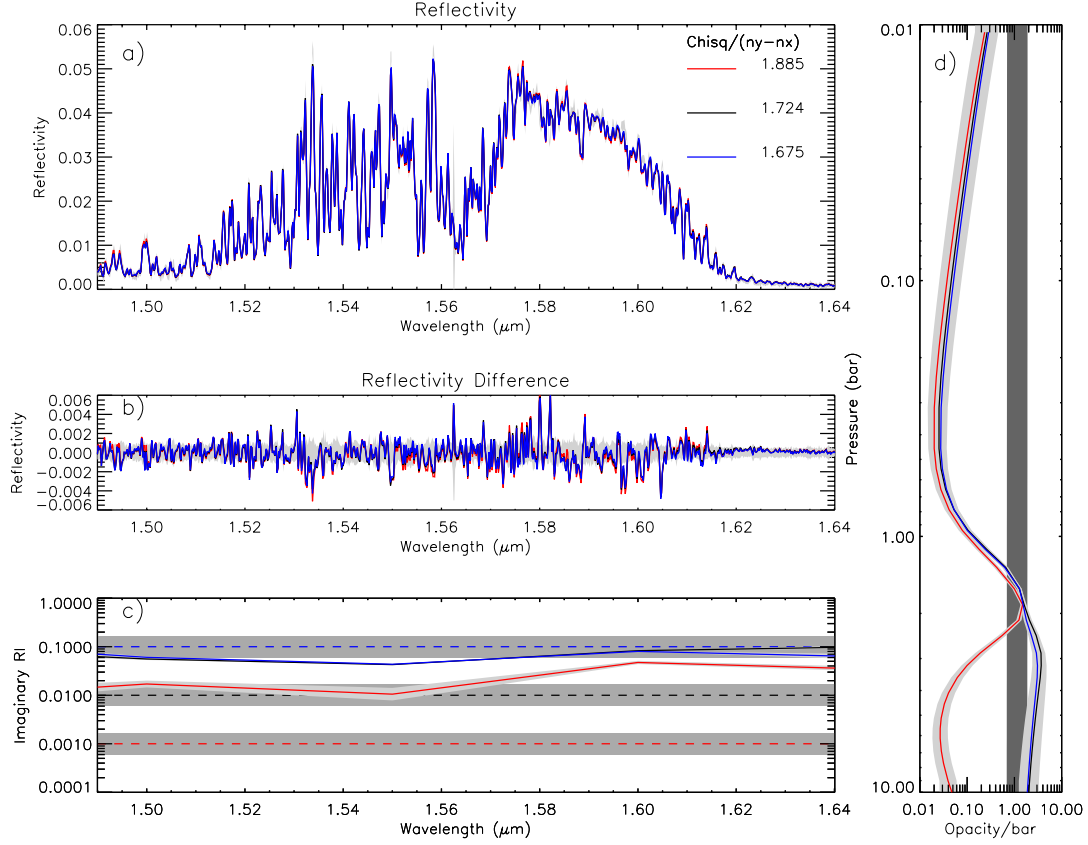


Figure 3: Fits to average Gemini/NIFS observation of Uranus, made on 2nd November 2010 at  $15.3^\circ$  N, using three different assumptions for the *a priori* imaginary refractive index spectrum, and excluding  $\text{H}_2\text{S}$  and  $\text{NH}_3$  absorption. The red line shows the results using  $n_i = 0.001 \pm 0.0005$ , the black line shows the results using  $n_i = 0.01 \pm 0.005$ , while the blue lines show the results using  $n_i = 0.1 \pm 0.05$ . Panel a) shows the fits to the measured spectra, panel b) shows the difference between the observed and modelled spectra. Panel c) shows the fitted imaginary refractive index spectra of the one type of particle assumed right hand plot, while panel d) shows the fitted cloud profiles (opacity/bar at  $1.6 \mu\text{m}$ ). In panels c) and d) the *a priori* value and range is marked in light grey, while the error range on the retrieved quantities is indicated in darker grey. The  $\chi^2/n$  of the fits is also shown in panel a).

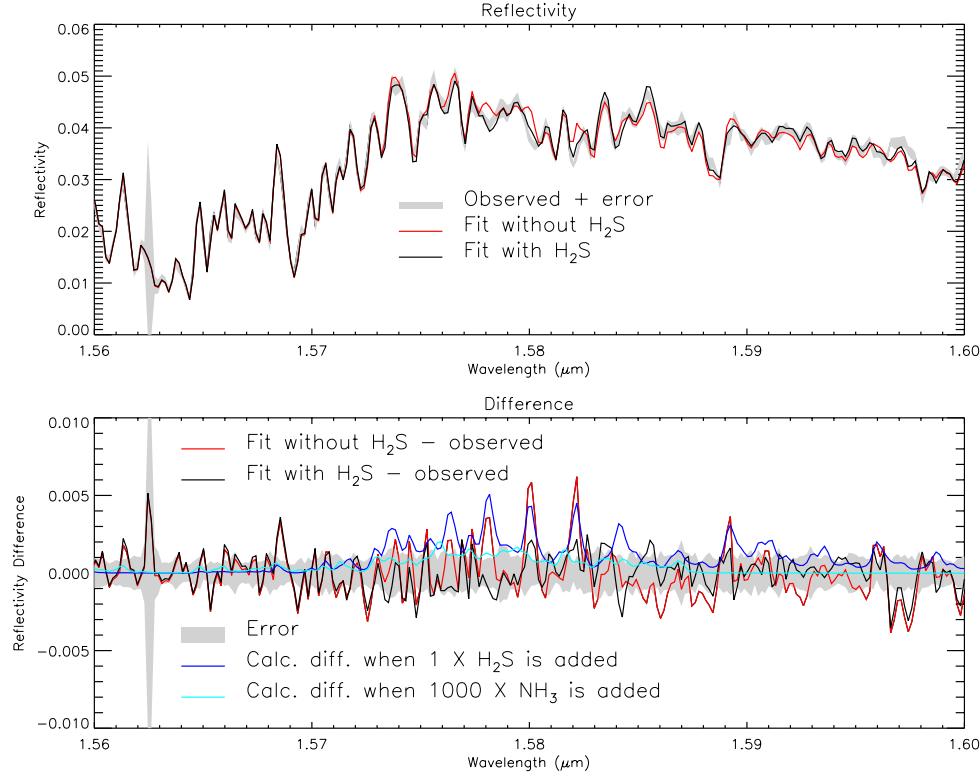


Figure 4: Fits to the co-added Gemini/NIFS observation of Uranus in the wavelength range 1.56 – 1.6  $\mu\text{m}$ . In the top plot, the observed reflectivity spectrum and estimated error is shown in grey. The fitted spectrum when  $\text{H}_2\text{S}$  absorption is not included is shown in red, while the fitted spectrum when  $\text{H}_2\text{S}$  absorption is included is shown in black. The bottom plot shows the differences between these fits and the observed spectrum using the same colours (i.e. red when  $\text{H}_2\text{S}$  absorption is not included and black when it is), with the error range again shown in grey. The blue line in the bottom plot shows how the calculated spectrum for the fit when  $\text{H}_2\text{S}$  absorption is not included (i.e. red line in the top plot) changes when  $\text{H}_2\text{S}$  absorption is added (leaving all other fitted parameters unchanged), assuming a profile with 100% relative humidity (RH). The cyan line shows how the calculated spectrum changes when  $\text{NH}_3$  absorption is added, leaving all other fitted parameters unchanged, assuming a profile with 1000 times the *a priori*  $\text{NH}_3$  profile with 100% RH.